Science Bulletin xxx (xxxx) xxx

Contents lists available at ScienceDirect

Science Bulletin

journal homepage: www.elsevier.com/locate/scib

Article

Rh/InGaN$_{1-x}$O$_x$ nanoarchitecture for light-driven methane reforming with carbon dioxide toward syngas

Yixin Li [a], Jinglin Li [a], Tianqi Yu [a], Liang Qiu [a], Syed M. Najib Hasan [d], Lin Yao [b,*], Hu Pan [a], Shamsul Arafin [d,*], Sharif Md. Sadaf [c,*], Lei Zhu [a], Baowen Zhou [a,*]

[a] Key Laboratory for Power Machinery and Engineering of Ministry of Education, Research Center for Renewable Synthetic Fuel, School of Mechanical Engineering, Shanghai Jiao Tong University, Shanghai 200240, China
[b] China-UK Low Carbon College, Shanghai Jiao Tong University, Shanghai 201306, China
[c] Centre Energie, Matériaux et Télécommunications, Institut National de la Recherche Scientifique (INRS)-Université du Québec, Varennes J3X 1E4, Canada
[d] Department of Electrical and Computer Engineering, The Ohio State University, Columbus, OH, 43210, USA

ARTICLE INFO

Article history:
Received 14 November 2023
Received in revised form 5 January 2024
Accepted 4 February 2024
Available online xxxx

Keywords:
Dry reforming of methane
Photo-thermal catalysis
Rh/InGaN$_{1-x}$O$_x$ nanowires

ABSTRACT

Light-driven dry reforming of methane toward syngas presents a proper solution for alleviating climate change and for the sustainable supply of transportation fuels and chemicals. Herein, Rh/InGaN$_{1-x}$O$_x$ nanowires supported by silicon wafer are explored as an ideal platform for loading Rh nanoparticles, thus assembling a new nanoarchitecture for this grand topic. In combination with the remarkable photo-thermal synergy, the O atoms in Rh/InGaN$_{1-x}$O$_x$ can significantly lower the apparent activation energy of dry reforming of methane from 2.96 eV downward to 1.70 eV. The as-designed Rh/InGaN$_{1-x}$O$_x$ NWs nanoarchitecture thus demonstrates a measurable syngas evolution rate of 180.9 mmol g_{cat}^{-1} h^{-1} with a marked selectivity of 96.3% under concentrated light illumination of 6 W cm^{-2}. What is more, a high turnover number (TON) of 4182 mol syngas per mole Rh has been realized after six reuse cycles without obvious activity degradation. The correlative ^{18}O isotope labeling experiments, *in-situ* irradiated X-ray photoelectron spectroscopy (ISI-XPS) and *in-situ* diffuse reflectance Fourier transform infrared spectroscopy characterizations, as well as density functional theory calculations reveal that under light illumination, Rh/InGaN$_{1-x}$O$_x$ NWs facilitate releasing $^*CH_3$ and H^+ from CH_4 by holes, followed by H_2 evolution from H^+ reduction with electrons. Subsequently, the O atoms in Rh/InGaN$_{1-x}$O$_x$ can directly participate in CO generation by reacting with the $^*C$ species from CH_4 dehydrogenation and contributes to the coke elimination, in concurrent formation of O vacancies. The resultant O vacancies are then replenished by CO_2, showing an ideal chemical loop. This work presents a green strategy for syngas production via light-driven dry reforming of methane.

1. Introduction

Considering the devastating impact of climate change, how to properly handle the two greenhouse gases such as carbon dioxide (CO_2) and methane (CH_4) has become one of the most critical issues in the twenty-first century [1–3]. Meanwhile, the depleting of crude oil poses a tremendous threat to the sustainable supply of transportation fuels and value-added chemicals [4]. Conversion of both CH_4 and CO_2 into syngas, namely dry reforming of methane (DRM), is considered as a proper solution for addressing the issues above [5–7]. However, CO_2 and CH_4 are chemically inert, requiring 805 and 440 kJ mol^{-1} to break the C=O and C–H bonds, respectively [8,9]. Extensive thermal energy is often required to achieve considerable reaction rates under high temperature (~700 °C) [10,11]. The pursuit of a green DRM route is highly desirable.

Photocatalysis presents a green means for driving chemical reactions under ambient conditions using solar energy. Over the past years, tremendous efforts have been devoted to exploring a range of photocatalysts for DRM [12–15]. Among the reported photocatalysts, metal oxides e.g., TiO_2, CeO_2, ZnO and MgO are extensively studied due to their low cost, chemical stability, and non-toxic feature [16–19]. However, even state-of-the-art photocatalysts are frequently limited by low activity. It is attributed to low photon absorption, severe e^-/h^+ recombination, and sluggish reaction kinetics arising from the inert nature of both CH_4 and CO_2. Thus far, there has been no virtual success in syngas production

* Corresponding authors.
E-mail addresses: yaol@sjtu.edu.cn (L. Yao), arafin.1@osu.edu (S. Arafin), sharif.sadaf@inrs.ca (S.Md. Sadaf), zhoubw@sjtu.edu.cn (B. Zhou).

https://doi.org/10.1016/j.scib.2024.02.020

Please cite this article as: Y. Li, J. Li, T. Yu et al., Rh/InGaN$_{1-x}$O$_x$ nanoarchitecture for light-driven methane reforming with carbon dioxide toward syngas, Science Bulletin, https://doi.org/10.1016/j.scib.2024.02.020

from light-driven DRM. Meanwhile, the photocatalysts are vulnerably deactivated owing to the accumulation of *C species from CH_4 dehydrogenation ($CH_4 \rightarrow C + 2H_2$) and CO disproportionation ($2CO \rightarrow C + CO_2$) on the surface [20–24]. What is more, the reaction mechanism of light-driven DRM has remained largely unknown. It is thus imperative to address the critical issues above.

InGaN nanowires (NWs) vertically aligned on a silicon wafer (InGaN NWs/Si), have emerged as a next-generation semiconductor platform for solar-to-fuels conversion because of the exceptional optoelectronic and catalytic properties [25–27]. Over recent years, a number of advances on solar fuels generation from water splitting and CO_2 reduction have been made by using InGaN NWs/Si [28–31]. From the viewpoint of catalysis, the unique N-rich surface of InGaN NWs is efficient for activating the inert CO_2 molecule according to the previous reports [29], especially if work in synergy with appropriate cocatalysts. Besides, Rh nanoparticles (NPs) are usually served as CH_4 activation sites according to its high catalytic activity and outstanding stability. However, to our best knowledge, there has been no endeavors in exploring a photocatalytic architecture for light-driven DRM by coupling Rh NPs with InGaN NWs.

In this study, an interesting Rh/$InGaN_{1-x}O_x$ nanoarchitecture supported by silicon wafer is explored for light-driven DRM toward syngas. Based on experimental and computational studies, it is revealed that Rh/$InGaN_{1-x}O_x$ enables efficient CH_4 activation. What is more, the O atoms in Rh/$InGaN_{1-x}O_x$ are directly involved in CO generation by reacting with the *C species from CH_4 deoxidation and contribute to the coke elimination, in concurrent formation of O vacancies (V_O). The formed V_O can be replenished by CO_2 through C=O bond cleavage, further contributing to CO evolution. It is noted that in the catalytic cycle, the concentrated light enables sufficient charges generation and high localized temperature of the catalytic architecture. A chemical loop is thus closed with significantly lowered apparent activation energy (E_a). As a result, Rh/$InGaN_{1-x}O_x$ nanoarchitecture demonstrates a high syngas evolution rate of 180.9 mmol g_{cat}^{-1} h^{-1} with a marked selectivity of 96.3% under light illumination of 6 W cm^{-2} without other extra energies. A considerable turnover number (TON) of 4182 mol syngas per mole Rh is achieved over 6 cycles of reuse without obvious activity degradation. What is more, concentrated light is beneficial for the reduced usage of photocatalyst, thus showing economic advantages. Overall, this study presents a promising strategy for DRM toward syngas with the input of light as the sole energy.

2. Experimental

2.1. Assembly of Rh/InGaN and Rh/$InGaN_{1-x}O_x$

MBE growth of InGaN NWs onto 4-inch Si wafer. The p-type doped GaN@InGaN single-band NW heterostructures were grown on Si substrate by Veeco Gen 930 plasma-assisted molecular beam epitaxy. The doping densities of p-type dopant in the p-GaN and p-InGaN regions were controllably tuned by controlling the Mg cell temperatures. During the growth, the plasma power was kept at 350 W, and NWs were grown in N-rich growth conditions. In and Ga beam equivalent pressure (BEPs) were carefully calibrated to tune the In composition range to cover the wider visible solar spectrum. The details of the growth condition can be found in the previous publication [32].

Immobilization of Rh NPs. The deposition of Rh NPs was carried out in a sealed Pyrex chamber with a quartz lid through a photodeposition process with a 300 W Xenon lamp as the light source. The wafer-scale InGaN NWs supported by Si were first cut into small pieces with a geometric surface of 0.2–0.5 cm^2. The small sample was then placed in the bottom of the chamber. Methanol (Ar, Sinopharm Chemical Reagent Company, China) aqueous solution with CH_3OH of 10 mL and H_2O of 50 mL was employed for photo-deposition. After that, a desired volume of Rh precursor ($Na_3RhCl_6{\cdot}xH_2O$, 99.99%, Shanghai Bailing Chemical Company, China) aqueous solution (concentration of 0.2 mol L^{-1} and the amount of 3–40 μL) was then added into the chamber, followed by vacuum to remove the air in the solution. The chamber was then filled with Ar and irradiated with the xenon lamp at a light intensity of 2 W cm^{-2} for 30 min to immobilize Rh NPs on the surface of InGaN NWs. The exact amount of the deposited Ru was determined by the inductive coupled plasma optical emission spectrometry (ICP-OES) technique. Rh/$InGaN_{1-x}O_x$ NWs were also fabricated by the same method as mentioned above; and the major difference was that $InGaN_{1-x}O_x$ NWs were obtained by InGaN NWs annealed under air at various temperature (300–800 °C) with a heating rate of 3 °C min^{-1} prior to the deposition of Rh. In this case, the nitrogen atoms of InGaN can be successfully substituted by oxygen under high temperature, enabling the achievement of $InGaN_{1-x}O_x$. The Rh/$InGaN_{1-x}{}^{18}O_x$ NWs were fabricated by annealing InGaN NWs under $^{18}O_2$ atmosphere at 600 °C for 1 h.

2.2. Characterization

A D8 Advance diffractometer (Bruker, Germany) with Cu Kα, at 60 kV and 80 mA was used for X-ray diffraction (XRD) patterns characterization. X-ray photoelectron spectroscopy (XPS) was measured by 250xi non-monochromatic (ESCALAB, USA) Al anodes, and the binding energy was corrected by using C 1s peak at 284.8 eV as the internal standard. The *in situ* irradiated XPS (ISI-XPS) was measured by 250xi non-monochromatic (ESCALAB, USA) Al anodes equipped with a 300 W Xe lamp as the light source. ICP measurements were performed using an ICP-OES (730, AGILENT, USA). Photoluminescence (PL) and time-resolved TR-PL spectra were collected by a FLS980 photoluminescence spectroscope (Edinburgh Instruments, UK). Thermal-gravimetry analysis (TGA) was tested by an STA 449 F3 Jupiter (NETZSCH, Germany) in the air. Scanning electron microscopy (SEM) images were obtained using a Quattro ESEM (ESCALAB, USA). High-angle annular dark field-scanning transmission electron microscopy (HAADF-STEM) images were captured by a Thermo Fisher Scientific Talos F200X S/TEM (ESCALAB, USA), equipped with a Super-X EDS detector and operated at 200 kV. TEM images were collected using a JEOL 2100F microscope (JEOL, Japan). *In situ* diffuse reflection infrared Fourier transform (DRIFT) spectroscopy was carried out using a Frontier FT-IR Spectrometer (PerkinElmer, USA), which was equipped with an MCT detector and 10-cm Demountable Gas Cell. A 315 infrared camera (POTRIC, China) was employed to detect the surface temperature of catalyst under the irradiation.

2.3. Performance evaluation

The syngas production from light-driven DRM was conducted in a home-made sealed Pyrex reaction chamber equipped with a quartz lid with the volume of 440 mL. The catalysts were thoroughly washed with deionized water before being fixed at the bottom of the Pyrex chamber, followed by vacuum. The chamber was then filled with atmospheric Ar. Subsequently, 120 mL Ar gas was extracted by a syringe, and 60 mL of CH_4 and 60 mL of CO_2 were injected into the reaction chamber, respectively. The reactions were carried out under light illumination by a 300 Xe lamp equipped with a lens and the illumination time was 30 min if not specifically noted. The optical intensity can be easily modulated by changing the current of the setup. The dark reaction was measured at an enclosed high-temperature tube furnace (NBD-HP1200). The tube was firstly filled with Ar after vacuum treatment, then 120 mL of Ar was withdrawn and 60 mL of CH_4 and

CO_2 were injected into the tube for the subsequent reactions. The heating rate was set as 3 °C min^{-1}. The gaseous products were finally analyzed by a gas chromatograph (GC-9080, Sun) equipped with a flame ionization detector (FID) detector and a thermal conductivity detector (TCD), respectively. Of note, the amount of InGaN NWs onto silicon wafer was estimated as follows: The cover factor of the InGaN NWs grown on Si wafer is about 70.3% over a 2.3 cm^2 piece as estimated by the photoshop software according to Fig. S1 (online). TheNWs illustrated an average length of 550 nm as measured by SEM technique (Fig. S2 online). The density of InGaN is about 6.1 g cm^{-3}. The weight of catalyst per unit area was thus calculated to be 0.235 mg cm^{-2} without considering the cocatalysts because of their low content.

The apparent quantum efficiency (AQE) was estimated as Eqs. (S7) and (S8) (online) [33], where the n represents the number of involved electrons, R is the evolution rate of syngas, I is the amount of incident protons, h is the the Plank constant, and c is the speed of light. All of the experiments were carried out under monochromatic light source which equipped with a quartz lens. The light intensities (P) of various wavelengths (λ) (275, 420, 535, and 730 nm) are 57.8, 315.5, 147.3, and 224.7 mW cm^{-2}, respectively. The light irradiation area (S) is 0.30 cm^2, which is the area of the $Rh/InGaN_{1-x}O_x$ NWs photocatalyst. The external temperature was controlled at 290 °C by a temperature tunable heating platform. The irradiation time (T) of the monochromatic light was 3600 s.

2.4. Computational methods

Density functional theory (DFT) calculations were performed employing the Vienna *Ab Initio* Simulation Package (VASP) [34,35]. The interaction between valence electrons and ions were described by the projector-augmented wave (PAW) method [36]. The exchange correlation of the Kohn-Sham equation was presented by generalized gradient approximation (GGA) with the Perdew-Burke-Ernzerhof (PBE) functional [37,38]. A plane-wave basic set was used to expand the wavefunctions with the kinetic cutoff energy set to 500 eV. For the calculations of slabs, a $2 \times 2 \times 1$ Mokhorst-Pack k-point grid was implemented to sample the Brillouin zone [39]. During the geometry optimization, the convergence criteria for the atomic forces and the total energies were set to 0.02 eV $Å^{-1}$ and 10^{-4} eV, respectively.

As the m-plane of InGaN was observed in experiments, we constructed InGaN(100) surface with a 4×3 supercell containing 6 layers to represent the pristine InGaN. Besides, Rh/InGaN and $Rh/InGaN_{1-x}O_x$ were created by depositing a small Rh10 cluster of metal atoms on InGaN(100). The top view, side view of optimized geometries of Rh10 clusters, InGaN(100), $InGaN_{1-x}O_x$(100), Rh/InGaN and $Rh/InGaN_{1-x}O_x$ are represented in Fig. S1 (online). To avoid image interaction, a vacuum spacing of at least 15 Å was set along the normal direction to the surface for all slab models and along all three directions for NPs. Moreover, for all slab models, the bottom three layers of InGaN were fixed in their bulk positions during structural relaxation.

3. Results and discussion

3.1. Adsorption behavior of CH_4 and CO_2 over Rh/InGaN and $Rh/InGaN_{1-x}O_x$

The adsorption behavior of both CH_4 and CO_2 plays a vital role in DRM. First of all, four surface models of Rh10 cluster, InGaN, $InGaN_{1-x}O_x$, Rh/InGaN, and $Rh/InGaN_{1-x}O_x$ are built by DFT calculations (Fig. S3 online). Based on the adsorption configuration and differential charge density analysis, it is seen that when CH_4 molecule is adsorbed on the Rh site of $Rh/InGaN_{1-x}O_x$ that serves a Lewis acid (Fig. S4 online). Moreover, the calculated adsorption energy (−0.921 eV) is obviously lower than that of −0.36 eV over pristine Rh/InGaN, suggesting effective interaction between CH_4 and $Rh/InGaN_{1-x}O_x$ (Fig. 1a, b). It facilitates the C–H bond cleavage of CH_4, thus lowering the activation energy of CH_4 dehydrogenation. The adsorption behavior of CO_2, a linear and inert reactant (C=O, 805 kJ mol^{-1}), was also studied. The lattice N was identified as the CO_2 adsorption sites for both Rh/InGaN and $Rh/InGaN_{1-x}O_x$ by serving as a Lewis base (Table S1 and Fig. S4 online). The adsorption energy was varied from −1.967 eV over Rh/InGaN to −1.342 eV $Rh/InGaN_{1-x}O_x$ (Fig. 1c, d). Moreover, on basis of charge density difference analysis, the incorporation of O into InGaN is favorable for the electron-density accumulation onto the N site, which will be verified by XPS characterization. Such an electronic variation facilitates the reaction by alternating the potential-determining step of CO_2 deoxidation, which will be studied in detail.

Temperature-programmed desorption (TPD) measurement was further conducted to study the adsorption behavior. Typically, the two peaks at the range of 150–250 and 300–500 °C could be attributed to the physical and chemical adsorption of CH_4, respectively (Fig. 1e) [40], being consistent with the DFT calculation (Fig. 1a, b). Compared to Rh/InGaN, $Rh/InGaN_{1-x}O_x$ exhibits a similar CH_4 desorption temperatures, illustrates that the introduction of O species did not change the adsorption strength significantly. However, an obvious increase of integral area of CH_4 desorption was observed for $Rh/InGaN_{1-x}O_x$, suggesting the increasing adsorption sites of CH_4 molecule. Besides, the peaks at the range of 100–250 and 320–450 °C could be attributed to the CO_2 desorption (Fig. 1f) [40]. The negative shift of desorption peak over $Rh/InGaN_{1-x}O_x$ shows a decreased adsorption strength of CO_2 molecule, which is in good agreement with the DFT calculations (Fig. 1c, d), confirming that the O atoms in $Rh/InGaN_{1-x}O_x$ can suitably weaken the interaction with CO_2 to participate in the subsequent activation reaction. DFT calculations and TPD characterizations above validate the feasibility of modulating the adsorption behavior of CH_4 and CO_2 by surface modification of InGaN, thus accelerating light-driven DRM toward syngas.

3.2. Assembly and characterization of $Rh/InGaN_{1-x}O_x$

The assembly of $Rh/InGaN_{1-x}O_x$ is schematically shown in Fig. 2a. With the use of a 4-inch Si(1 1 1) wafer as substrate, InGaN NWs were grown by plasma-assisted molecular beam epitaxy (MBE) under N_2-rich atmosphere based on the reported literature [41]. Herein, the epitaxial InGaN NWs are thermally stable owing to the high grown temperature. Meanwhile, the surface of InGaN NWs is predominantly terminated with nitrogen atoms. It thus offers a suitable platform for assembling a high-temperature-tolerant photocatalytic architecture. $Rh/InGaN_{1-x}O_x$ was then assembled through a combination of photo-depositing Rh NPs with annealing. As characterized by SEM, $Rh/InGaN_{1-x}O_x$ NWs show an average length of 600–700 nm with diameter between 70 and 100 nm vertically distributed on Si wafer (Fig. 2b). The one-dimensional (1-D) morphology of InGaN did not exhibit a noticeable change after annealing (Fig. S2 online). Based on the TEM characterization, it was found that Rh NPs were uniformly distributed on the NW surface (Fig. 2c). HAADF-STEM characterization, in combination with the energy-dispersive X-ray spectroscopy (EDX) elemental mapping images, showed the uniform distribution of In, Ga, N, Rh and O element (Fig. 2d, e). Moreover, the interplanar distances of 0.221 and 0.253 nm are indexed to Rh(1 1 1) and $Rh/InGaN_{1-x}O_x$(002), respectively. It is noted that, as characterized by electron spin resonance (ESR) spectroscopy, compared to Rh/InGaN NWs, a typical single-electron-trapped lattice oxygen signal with a g-factor of 2.003 was detected for $Rh/InGaN_{1-x}O_x$ NWs [42], suggesting the virtual success in substituting N of InGaN with O (Fig. 2f). By XRD spectroscopy technique (Fig. S5 online), all the sam-

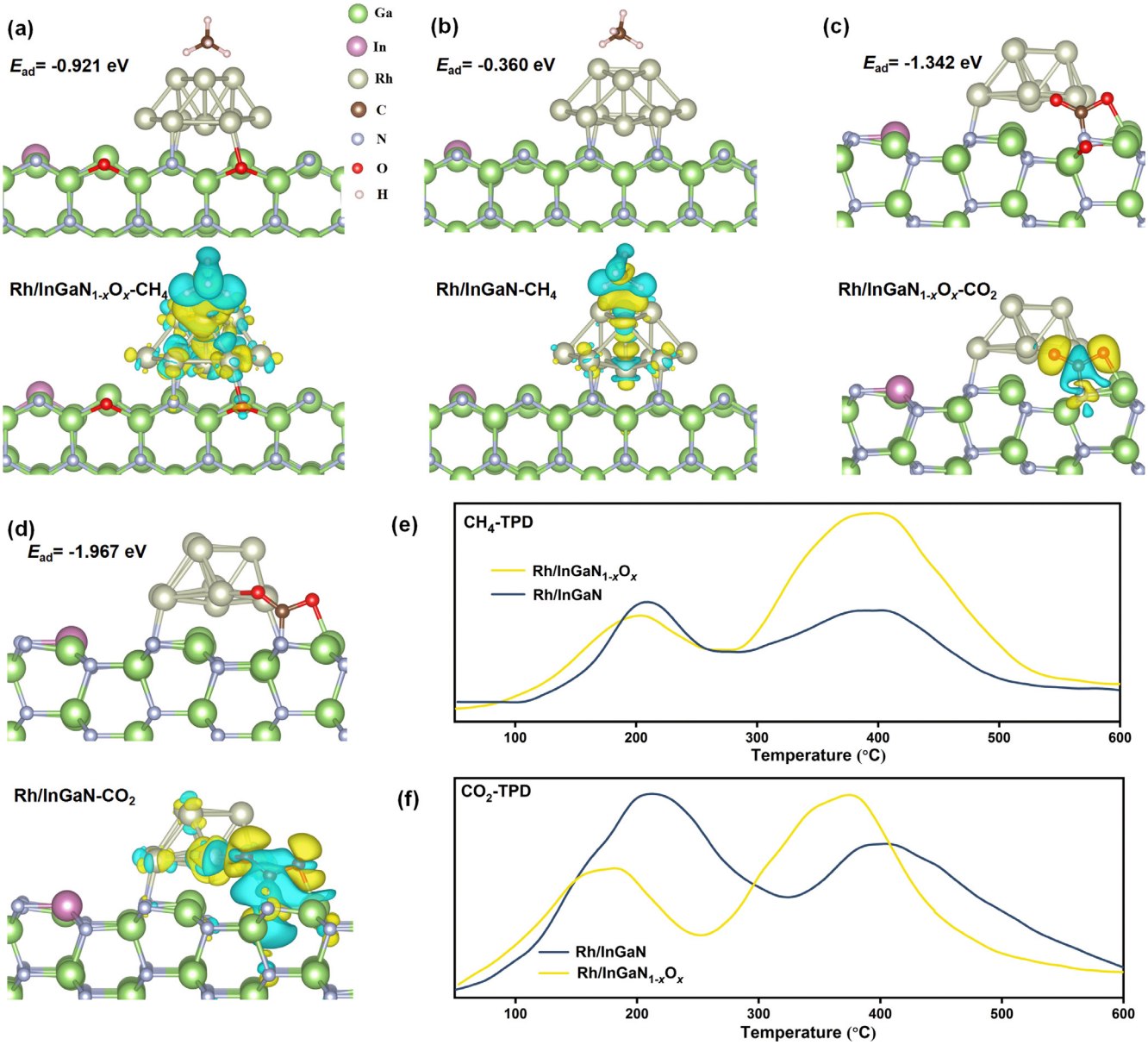

Fig. 1. Adsorption behavior of CH_4 and CO_2 over Rh/InGaN and Rh/InGaN$_{1-x}$O$_x$. CH_4 adsorption configuration (top) and charge density difference (bottom) of (a) Rh/InGaN$_{1-x}$O$_x$ and (b) Rh/InGaN. CO_2 adsorption configuration (top), charge density difference (bottom) of (c) Rh/InGaN$_{1-x}$O$_x$ and (d) Rh/InGaN. (e) TPD spectra of CH_4 desorption behavior. (f) TPD spectra of CO_2 desorption behavior. Ga, green; N, silver; In, purple; Rh, gray; O, red. Regions of yellow and cyan indicate the gain and loss of electronic charge respectively, with an isosurface of 0.003 e Å^{-1}.

ples tested exhibited typical diffraction peaks of the (002) plane of InGaN at 2θ of 34.14°, suggesting that the *c*-axis growth direction of InGaN NWs. The annealing did not affect the crystal structure of InGaN NWs a lot. Moreover, the characteristic peak of Rh did not appear in the XRD patterns owing to the low loading content, which was measured to be 0.04 μmol cm^{-2} by ICP-OES.

The electron-hole recombination of both InGaN and InGaN$_{1-x}$O$_x$ can be significantly inhibited by decorating with Rh NPs, as characterized byPL spectroscopy (Fig. S6 online). Differential ultraviolet–visible–infrared (UV–Vis-IR) spectroscopy measurement illustrated that the introduction of O enabled the optical improvement at the ultraviolet range, which is favorable for generating energetic charge carriers, thus facilitating the reaction (Fig. S7 online). In addition, the band gap was estimated to be 2.9 eV (Fig. S8 online), being well matched with the PL result. Moreover, TRPL illustrated that the charge lifetime of InGaN$_{1-x}$O$_x$ could be extended by the incorporation of Rh NPs, thus benefiting the reaction (Fig. 1g).

The surface chemical compositions of Rh/InGaN and Rh/InGaN$_{1-x}$O$_x$ were studied by XPS (Fig. S9 online). A typical Ga–O peak was detected at 24.3 eV in Ga 3d XPS spectra of Rh/InGaN$_{1-x}$O$_x$ (Fig. 2h) [43]. Meanwhile, a negative binding energy shift was seen for N 1s in Rh/InGaN$_{1-x}$O$_x$ (Fig. 2i). Moreover, the positive shift of Rh 3d and O 1s were observed for Rh/InGaN$_{1-x}$O$_x$ compared to Rh/InGaN (Fig. 2j, k) [43]. Therefore, the incorporation of O into Rh/InGaN facilitated the electron accumulation onto the N site. Such an electronic variation is of benefit for CO_2 activation since the N site is identified as a CO_2 adsorption site [44].

3.3. Performance of light-driven syngas production from CH_4 and CO_2 over Rh/InGaN$_{1-x}$O$_x$ NWs

The reactions were carried out in a home-made sealed quartz chamber illuminated by a 300 W xenon lamp equipped with a lens. At first, as shown in Fig. 3a, Rh/InGaN NWs showed a moderate

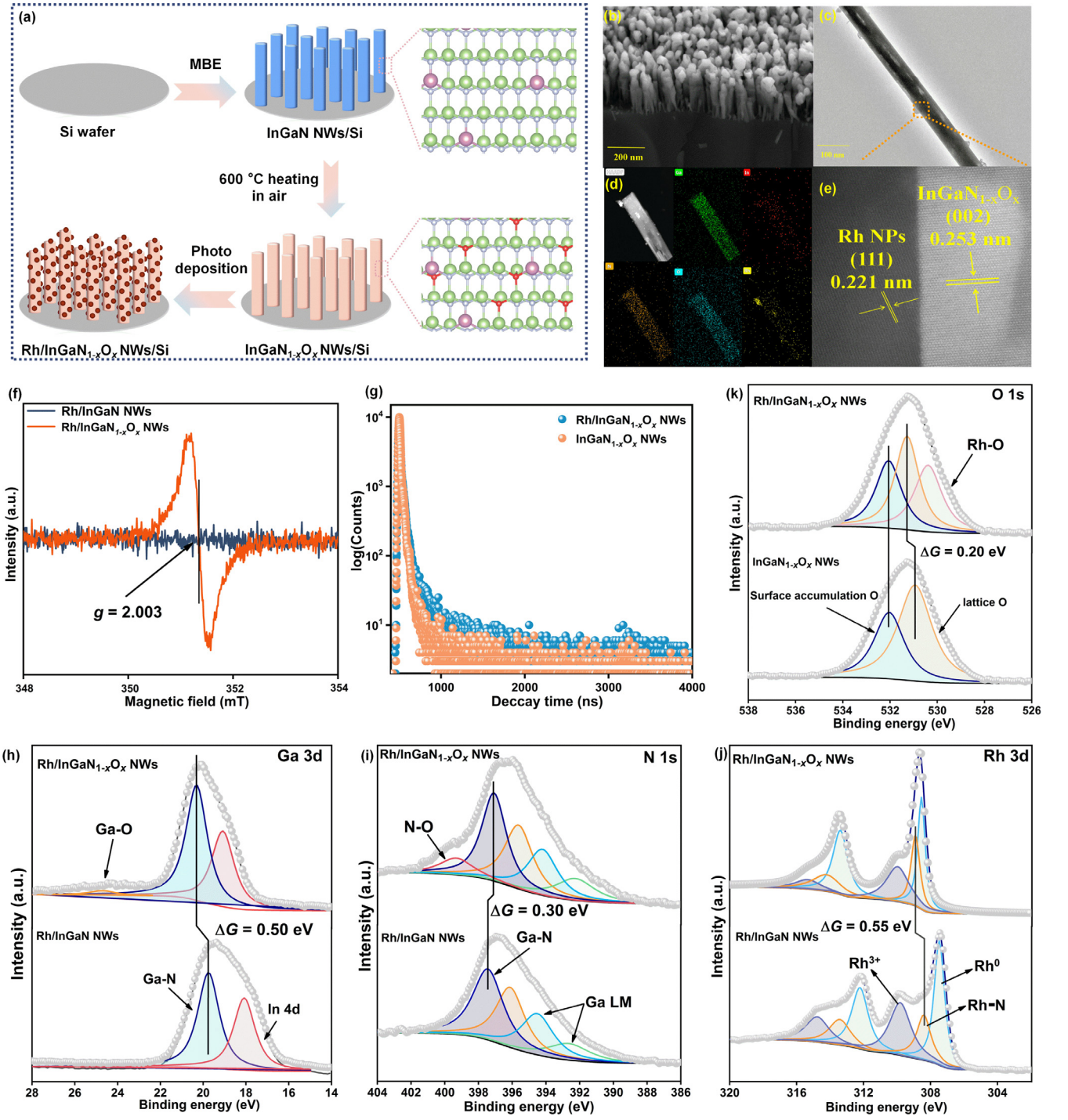

Fig. 2. Assembly and characterization of Rh/InGaN$_{1-x}$O$_x$. (a) Schematic illustration of the assembly of Rh/InGaN$_{1-x}$O$_x$ NWs by combining plasma-assisted MBE growth of InGaN NW and high-temperature calcination, followed by photo-deposition of Rh. Ga, green; N, silver; In, purple, O, red. (b) A 45° tilted-SEM image of Rh/InGaN$_{1-x}$O$_x$ NWs/Si. (c) TEM image of a single NW of Rh/InGaN$_{1-x}$O$_x$. (d, e) HAADF-STEM and EDS mapping images of Rh/InGaN$_{1-x}$O$_x$. (f) ESR spectra of Rh/InGaN$_{1-x}$O$_x$ NWs and Rh/InGaN NWs. (g) TR-PL spectrum of Rh/InGaN$_{1-x}$O$_x$ NWs and InGaN$_{1-x}$O$_x$. High-resolution XPS spectra of (h) Ga 3d, (i) N 1s, (j) Rh 3d of Rh/InGaN and Rh/InGaN$_{1-x}$O$_x$ (k) O 1s of InGaN$_{1-x}$O$_x$ and Rh/InGaN$_{1-x}$O$_x$.

syngas activity of 9.9 mmol g_{cat}^{-1} h^{-1} under concentrated light illumination of 5 W cm^{-2}, suggesting the viability of using InGaN NWs as scaffold for light-driven DRM. The obtained H_2/CO ratio of 0.55 is far away from the stoichiometric ratio of 1:1 ($CH_4 + CO_2 = 2CO + 2H_2$). It is indicative of a low atom utilization efficiency. In sharp contrast, Rh/InGaN$_{1-x}$O$_x$ nanoarchitecture showed an obvious enhancement in both syngas activity and H_2/CO ratio. Nevertheless, the H_2/CO ratio is still below 1, which is mainly due to the undesired reverse water gas shift (RWGS) reaction ($CO_2 + H_2 = CO + H_2O$) as verified by the spectroscopic characterizations next. In detail, the activity of syngas increased with the calcination temperature and reached a maximum value of 124.3 mmol g_{cat}^{-1} h^{-1} after 1 h sintering at 600 °C. Correspondingly, the H_2/CO ratio approached to 0.89. Moreover, the syngas evolution over Rh/

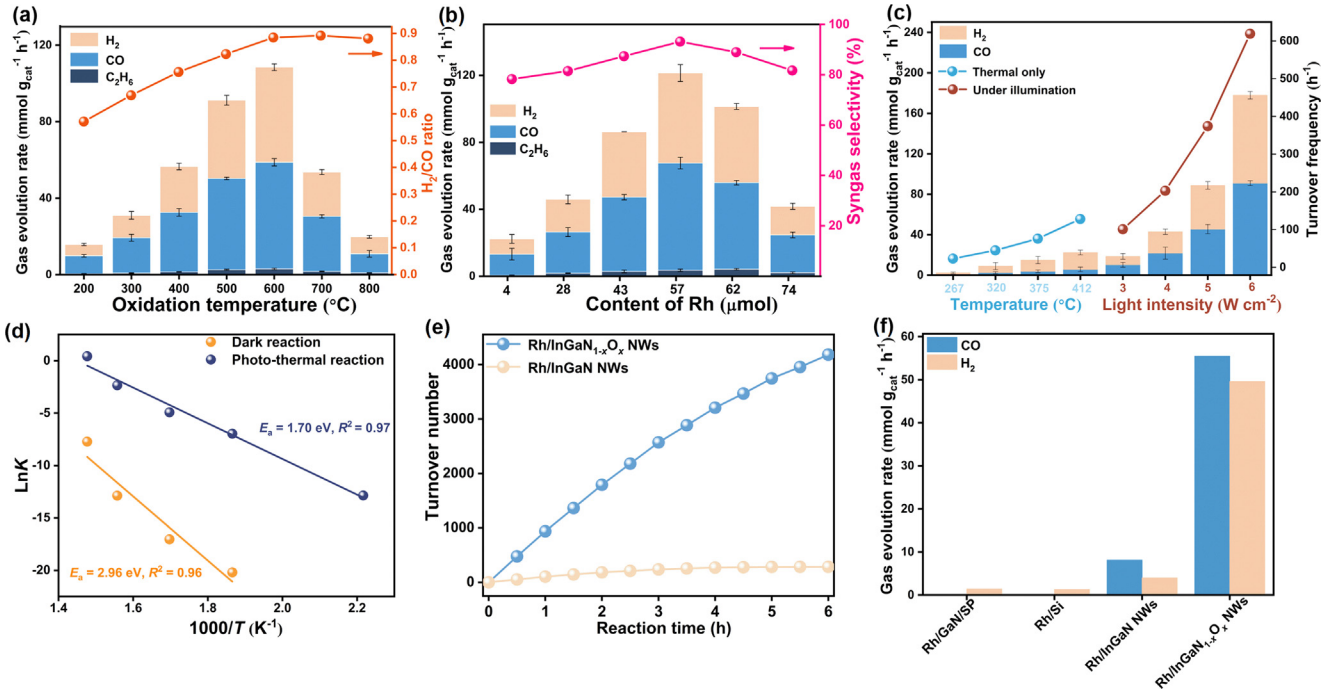

Fig. 3. Performance of light-driven syngas production from CH_4 and CO_2 over Rh/InGaN$_{1-x}$O$_x$. NWs influence of (a) annealing temperature and (b) Rh content on the performance of Rh/InGaN$_{1-x}$O$_x$. (c) Performance comparison between thermal catalytic and light-driven DRM toward syngas over Rh/InGaN$_{1-x}$O$_x$ NWs. (d) Activation energy of thermal-catalytic and light-driven DRM over Rh/InGaN$_{1-x}$O$_x$ NWs. (e) TON of Rh/InGaN NWs and Rh/InGaN$_{1-x}$O$_x$ NWs under light illumination. (f) DRM performance of Rh NPs deposited on various substrates. Reaction conditions: Light intensity is 5 W cm^{-2} for Fig. 3a, b, and 6 W cm^{-2} for Fig. 3c, d; the area of photocatalyst is about 0.5 cm^2; the reactor volume is 440 mL; CH_4:CO_2:Ar = 1:1:2 (volume ratio); atmospheric pressure; reaction time is 30 min.

InGaN$_{1-x}$O$_x$ exhibited a dramatic reduction when the calcination was operated at temperatures higher than 600 °C. The calcination time also exerted an evident impact on the performance. As shown in Fig. S10 (online), when InGaN was annealed at 600 °C for 0.5 h, the as-prepared Rh/InGaN$_{1-x}$O$_x$ showed a considerable syngas rate of 180.9 mmol g_{cat}^{-1} h^{-1}. It is an order magnitude higher than that of Rh/InGaN and outstrips the activity of most of the previous studies under the similar reaction conditions (Table S2 online). The results above unambiguously suggest that Rh/InGaN$_{1-x}$O$_x$ is superior to Rh/InGaN for syngas production from CH_4 and CO_2 via DRM under concentrated light illumination. The syngas activity was then quantitatively correlated with the calcination by XPS (Fig. S11 and Table S3 online). As expected, the O content of Rh/InGaN$_{1-x}$O$_x$ was elevated by increasing the annealing temperature and time, thus limiting the CO_2 adsorption/activation on N sites (Fig. S2 online). The activity was accordingly reduced. As a key component of the architecture, the loading of Rh NPs was also optimized (Fig. 3b). An optimal syngas activity of 123.7 mmol g_{cat}^{-1} h^{-1} with a marked selectivity of 96.3% was achieved at a Rh content of 0.057 μmol cm^{-2} under light illumination of 5 W cm^{-2}. The syngas evolution rate dramatically declined to 44.4 mmol g_{cat}^{-1} h^{-1} by increasing the Rh content to 0.074 μmol cm^{-2}. As shown in Fig. S12 (online), the particle size has a slight increase by varying the amount of Rh precursor from 3 to 40 μL. Therefore, the decreased activity is primarily associated with the light-shielding effect caused by the intensive loading of Rh [45].

The activity of Rh/InGaN$_{1-x}$O$_x$ NWs was estimated under various conditions. Considering the remarkable thermal effect of concentrated light, the surface maximum temperature (T_{max}) of Rh/InGaN$_{1-x}$O$_x$ supported by silicon wafer under various light intensities was first recorded by an infrared thermal camera, showing an increasing trend from 267 °C at 3 W cm^{-2} light illumination up to 412 °C at 6 W cm^{-2} (Fig. S13 online). Subsequently, the pure thermal-catalytic performance was compared with the activity recorded under concentrated light illumination, in order to investigate the origin of the superior activity. As shown in Fig. 3c, the syngas evolution rates of Rh/InGaN$_{1-x}$O$_x$ NWs under concentrated light illumination without external thermal energy far outperform its pure thermal-catalytic activity under the same temperature. In particular, for pure thermal-catalysis, the syngas evolution rate of Rh/InGaN$_{1-x}$O$_x$ is as low as 32.4 mmol g_{cat}^{-1} h^{-1} at 412 °C (T_{max} recorded at 6 W cm^{-2}), which is 17.9% of the activity recorded at 6 W cm^{-2}. As estimated by Arrhenius equation, the apparent activation energy (E_a) dropped from 2.96 eV downward to 1.7 eV upon illumination compared to thermal-catalysis (Fig. 3d) [46,47]. To further decouple the critical role of photon and heat in the photo-thermal catalytic DRM reaction under concentrated light illumination. The AQE was evaluated under various monochromic light illumination equipped with an external heater (Fig. S14 online). It is discovered that the AQE of Rh/InGaN$_{1-x}$O$_x$ NWs reaches 8.36% when illuminated by a 275 nm monochromatic light source under 290 °C. However, without varying the chamber temperature, the AQE demonstrated a decreasing trend as the light wavelength increased. When illuminated by a 730 nm monochromic light, the activity is nearly the same as its pure thermal-catalysis since the semiconductor can not be excited, as suggested by the PL measurement. These findings clearly show that photo-thermal synergy under concentrated light illumination is critical for the achievement of highly efficient syngas generation from DRM by providing energetic charge carriers and high localized temperature.

The durability was further tested (Fig. S15 online). It was found that there is a slight activity degradation after 6 cycles of operation over Rh/InGaN$_{1-x}$O$_x$ NWs, indicating an appreciable stability. In contrast, Rh/InGaN NWs illustrated a dramatic activity degradation under the same measured conditions. However, as characterized

by the TEM technique in Fig. S16 (online), after 6 cycles of stability test, an agglomeration of Rh NPs was indeed observed, which is associated with the high temperature arising from the concentrated light illumination condition, thus leading to the activity degradation. It is well consistent with the reported study. By XPS characterization, it was found that the coking rate of Rh/InGaN NWs was faster than that of Rh/$InGaN_{1-x}O_x$ NWs (Fig. S17 online), which can be due to the eventual CH_4 dehydrogenation ($CH_4 \rightarrow C + 2H_2$) and CO disproportionation ($2CO \rightarrow C + CO_2$). Therefore, the partial substitution of N of InGaN with O contributed to a notable stability by inhibiting coke deposition (Table S4 online), as elaborated next. Consequently, Rh/$InGaN_{1-x}O_x$ NWs demonstrated a TON of 4182 mol syngas per mole Rh after 6 cycles of reuse over 6 h, far exceeding that of Rh/InGaN (Fig. 3e). When Rh NPs were directly deposited on bare Si and GaN thin film supported by sapphire, the syngas activity was much lower than that of both Rh/InGaN and Rh/$InGaN_{1-x}O_x$ (Fig. 3f). This result suggests the critical role of 1-D InGaN NWs in the success of syngas production via DRM. In particular, 1-D InGaN NWs supported by silicon wafer enabled alleviating light scattering, facilitating efficient e^-/h^+ separation, and efficient active sites exposure, thus maximizing the activity of light-driven DRM. Control experiments by only feeding CH_4 or CO_2 did not show an obvious yield of syngas, validating that syngas was primarily produced from CH_4 and CO_2 via DRM (Fig. S18 online).

3.4. Studies of reaction mechanism of light-driven DRM toward syngas over Rh/$InGaN_{1-x}O_x$ NWs

It is vital to reveal the reaction mechanism. Herein, an isotope labeling experiment was first conducted to uncover the underlying mechanism of DRM with CO_2 toward CO/H_2 over Rh/$InGaN_{1-x}O_x$. Typically, ^{18}O-labelled Rh/$InGaN_{1-x}{}^{18}O_x$ was prepared by annealing InGaN under $^{18}O_2$ atmosphere, followed by the deposition of Rh NPs. The as-prepared Rh/$InGaN_{1-x}{}^{18}O_x$ nanoarchitecture was employed for DRM under light illumination of 5 W cm^{-2}. Strikingly, $C^{18}O$ was detected by gas chromatography-mass spectrometer (GC–MS), validating that the O atoms in ^{18}O-labelled Rh/$InGaN_{1-x}{}^{18}O_x$ directly participated in the formation of CO during the reaction, accompanied by the generation of V_O. Nevertheless, CO was mainly produced from the C=O cleavage of CO_2.

Specifically, as characterized by high-resolution XPS O 1s spectra in Fig. S19 (online), the deconvolution peak of 530.8 eV is attributed to the interaction of O and Rh atoms. Further, there was no obvious variation in the lattice oxygen content for Rh/$InGaN_{1-x}O_x$ NWs after the reaction. Thereby, it is rationally speculated that Vo can be favorably replenished by oxygen from the C=O cleavage of CO_2, enabling a chemical loop with concurrent formation of $C^{16}O$. It was validated by the GC–MS characterization shown in Fig. 4a. What is more, as characterized by thermogravimetric (TG) measurement (Fig. 4b), the coking content of Rh/InGaN NWs reached 0.71%, which was fiercer than that of 0.35% over Rh/$InGaN_{1-x}O_x$ NWs under the same conditions (Fig. S17 online). In combination with the O^{18}-labelled isotope labeling experiments, it is rational that the O atoms in Rh/$InGaN_{1-x}O_x$ are prone to eliminate the C species from CH_4 dehydrogenation. It thus favored the stability of DRM by inhibiting coke deposition. Furthermore, *in-situ* irradiated X-ray photoelectron spectroscopy (ISI-XPS) characterization was conducted to explore the charge transfer behavior of Rh/$InGaN_{1-x}O_x$ under light illumination. As shown in Fig. 4c, there was a positive binding energy shift occurring for Rh 3d under light illumination, illustrating the redistribution of photoexcited electron from Rh to $InGaN_{1-x}O_x$ NWs. Moreover, a negative binding energy shift of N 1s and a positive binding energy shift of O 1s were simultaneously observed under light irradiation (Fig. S20 online) [48]. Therefore, the O atoms in Rh/$InGaN_{1-x}O_x$ facilitate the redistribution of electrons from Rh to the N sites, which is favorable for the subsequent CO_2 activation. *In-situ* DRIFT spectroscopy was also conducted to study the key intermediates of the reaction (Fig. 4d). The apparent peaks at 1303 cm^{-1} and in the range of 2216–2394 cm^{-1} are attributed to the adsorbed CH_4 and CO_2 on the Rh surface and N sites of InGaN, respectively [49]. In addition, the peaks at 1008 and 1532 cm^{-1} can be assigned to the formation of carbonate, illustrating the activation of CO_2 molecules [49]. Under light illumination, the typical peak of *CO was observed at 2260 cm^{-1} after 5 min of the reaction [50]. Meanwhile, the peak at 1347 cm^{-1} can be indexed to the deformation vibrations of the adsorbed $*CH_3$ intermediate from CH_4 deprotonation [50] while the C−H stretching vibration peaks of $*CH_2$ and *CH were detected at 3133–3415 cm^{-1} [51]. It indicates that the adsorbed CH_4 is gradually dehydrogenated to form the $*CH_x$ and *H by photoexcited holes under light illumination. The released protons can be consumed for H_2 evolution using photoexcited electrons. $\bullet CH_3$ [52] was detected by *in-situ* electron paramagnetic resonance (EPR) spin-trapping technique (Fig. S21 online), further validates the success in CH_4 deprotonation by photoexcited holes over Rh/$InGaN_{1-x}O_x$. In addition, the typical •OH peaks gradually increased in the range of 3560–3764 cm^{-1} as the reaction progressed to 10 min, confirming the occurrence of RWGS reaction [50]. The aforementioned information draws the basic reaction profile for light-driven DRM ($CH_4 + CO_2 \rightarrow CO + H_2$) over Rh/$InGaN_{1-x}O_x$.

3.5. DFT calculations

DFT calculations were conducted to study the reaction mechanism at the molecular level. As indicated by the calculated free energy diagram, for CH_4 dehydrogenation, the potential-determining step ($*CH_4 \rightarrow *CH_3 + *H$) was not varied with the incorporation of O into Rh/InGaN (Fig. 5a). It is associated with the difficulty in breaking the first C–H bond arising from the inertness of CH_4. However, the energy barrier of the potential-determining step can be significantly lowered from 1.06 eV over Rh/InGaN downward to 0.842 eV over Rh/$InGaN_{1-x}O_x$. Subsequently, the formed $*CH_3$ species continues to release protons and eventually produces *C species. In addition, the *C also can be formed from the produced CO ($2CO \rightarrow C + CO_2$). For Rh/$InGaN_{1-x}O_x$, the adsorbed *C species are prone to migrate to the top site of Rh atoms, which is adjacent to the O atoms (Fig. S22 online), thus facilitating the subsequent formation of CO. It is absolutely different from the observation in Rh/InGaN, wherein the adsorbed *C species are more likely to migrate to the fcc plane of the Rh NPs (Fig. S23 online). The evolution track of CO_2 was also investigated. As illustrated in Fig. 5b, when a CO_2 molecule is adsorbed on the Rh/InGaN interface, a relatively high energy barrier of 1.906 eV is required to break the inert C=O bond of CO_2 (Fig. S23 online). In contrast, Rh/$InGaN_{1-x}O_x$ NWs are able to directly produce CO by combining with the *C species, showing a significantly reduced energy barrier of 0.537 eV. V_O was consequently produced after the release of CO* (Fig. S22 online). The resultant V_O can be replenished by CO_2 via C=O cleavage to close the chemical loop with a moderate energy barrier of 1.136 eV. The resultant *CO species that adsorbed over the interface can be further evolved toward CO, which has been verified by the GC–MS characterization in Fig. 4a. CO desorbed on the Rh metal surface, as an important kinetic step for syngas production in DRM due to its strong adsorption on metal surface, is also shown in Fig. 5b. It can be found that the *CO formed by the cleavage of the C=O of CO_2 over either Rh/InGaN or Rh/$InGaN_{1-x}O_x$ is more inclined to desorb on the surface of InGaN firstly, requiring 0.708 and 0.532 eV, respectively. Subsequently, for Rh/$InGaN_{1-x}O_x$, the energy barrier of *CO desorption on the Rh surface is 0.993 eV, which is significantly smaller than that of

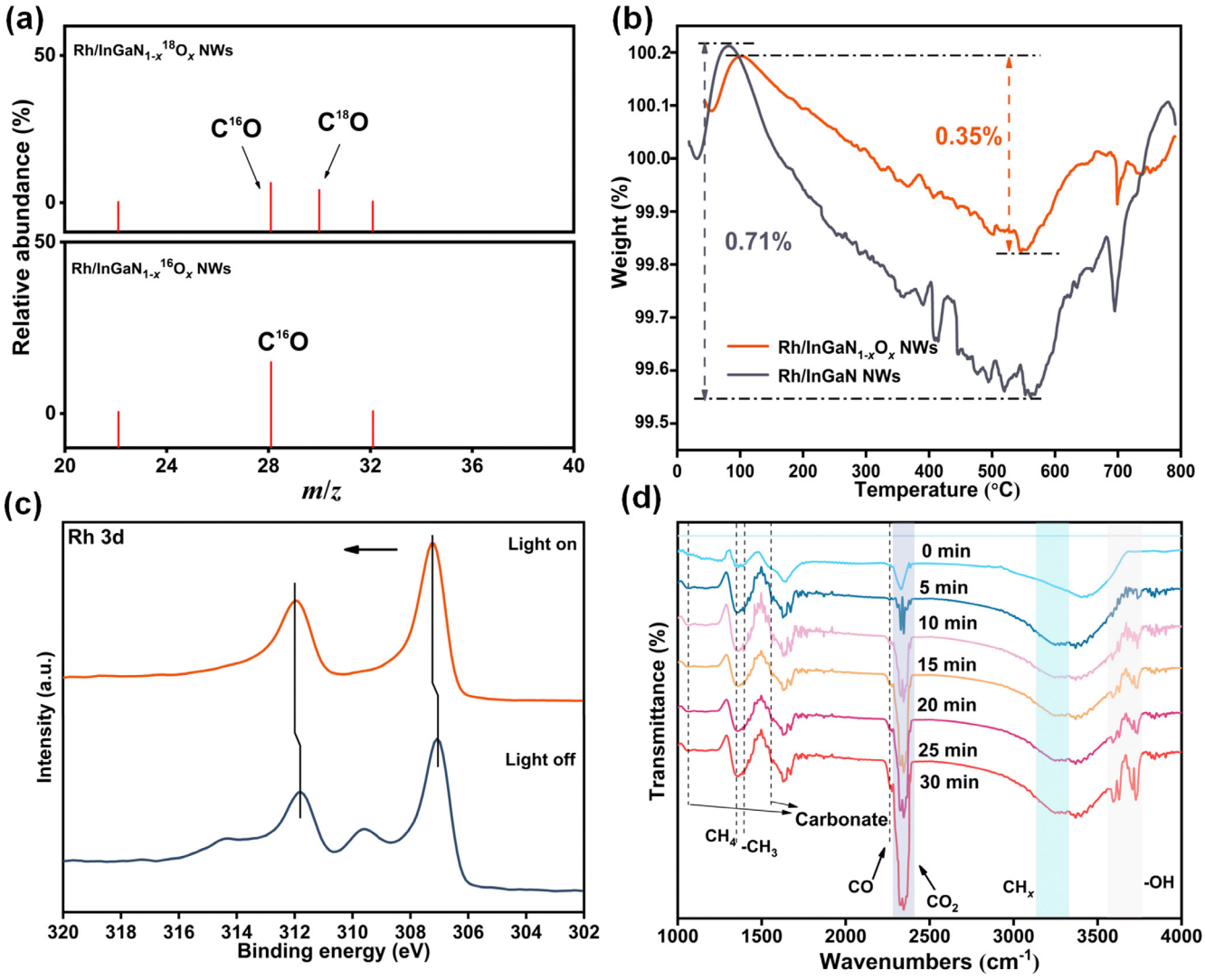

Fig. 4. Studies of reaction mechanism of light-driven DRM toward syngas over $Rh/InGaN_{1-x}O_x$ NWs. (a) Gas chromatography-mass spectra of CO produced from CH_4 and CO_2 over O^{18}-labeled $Rh/InGaN_{1-x}{}^{18}O_x$ NWs and $Rh/InGaN_{1-x}O_x$ NWs. (b) TG curves of $Rh/InGaN_{1-x}O_x$ NWs and Rh/InGaN NWs after 6 cycles of reuse for light-driven DRM. (c) ISI-XPS spectra of Rh 3d of $Rh/InGaN_{1-x}O_x$ NWs (the testing condition: 300 W xenon lamp, light illumination, 6 W cm^{-2}, feedstock, CO_2:CH_4:Ar = 1:1:2). (d) *In-situ* DRIFT spectra of syngas production from CH_4 and CO_2 over $Rh/InGaN_{1-x}O_x$ NWs under light illumination of 6 W cm^{-2}.

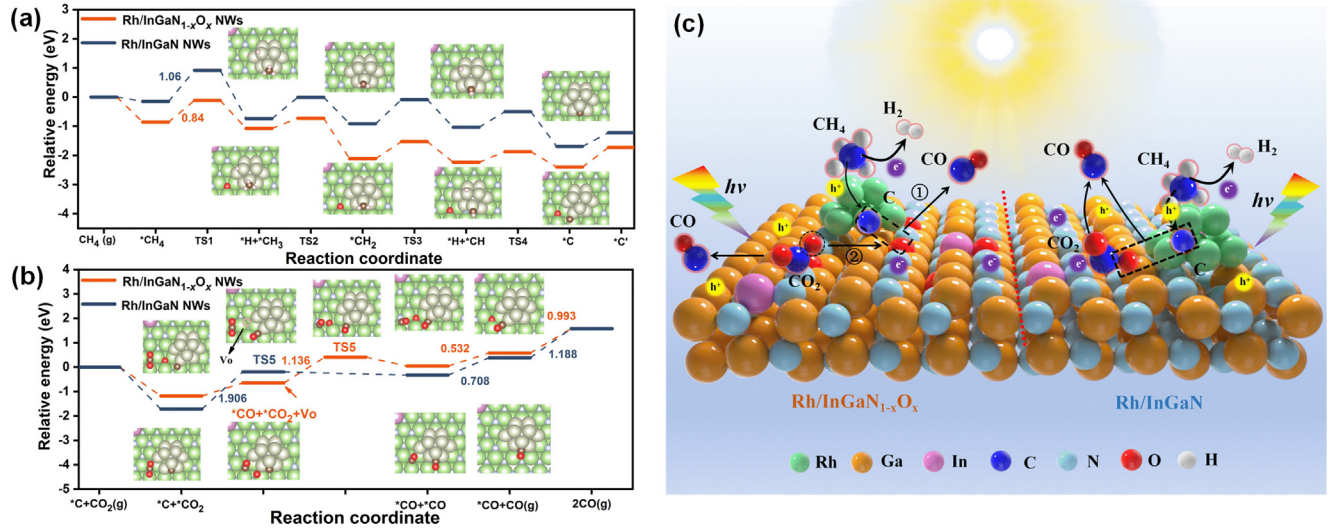

Fig. 5. DFT calculations. The calculated free energy diagrams for (a) CH_4 dehydrogenation, (b) CO_2 deoxidation on $Rh/InGaN_{1-x}O_x$ NWs and Rh/InGaN NWs respectively. Ga, green; N, silver; In, purple; Rh, gray; O, red. (c) Schematic diagram of DRM reaction mechanisms over Rh/InGaN NWs and $Rh/InGaN_{1-x}O_x$ NWs, respectively.

1.188 eV of Rh/InGaN. The lower desorption energy barrier of *CO is also one of the important reasons for the excellent activity of DRM reaction for Rh/InGaN$_{1-x}$O$_x$. What is more, DFT calculations showed that the reverse water gas shift reaction is not energetically favorable over Rh/InGaN$_{1-x}$O$_x$, which is beneficial for the achievement of a high H_2/CO ratio (Figs. S24 and S25 online). Based on the discussion above, the mechanism is proposed (Fig. 5c). Under light irradiation, CH_4 molecules are dehydrogenated by photoexcited holes to form *C species, accompanied by the release of protons. The O atoms in Rh/InGaN$_{1-x}$O$_x$ directly participate in CO generation by reacting with the *C species and contribute to the coke elimination, in concurrent formation of V_O (Fig. 5c, left, step ①). The released protons from CH_4 are reduced by the photoexcited electrons toward H_2. The V_O are then replenished by the O atom in CO_2 (Fig. 5c, left, step ②), being another origin of CO evolution. Together, partially substituting N of InGaN with O results in a substantial leap in activity and stability of light-driven DRM in the presence of Rh.

4. Conclusion

In summary, a novel Rh/InGaN$_{1-x}$O$_x$ nanoarchitecture was successfully assembled for light-driven syngas production from CH_4 and CO_2. The O atoms in Rh/InGaN$_{1-x}$O$_x$ were validated to significantly lower the activation energy from 2.96 eV downward to 1.70 eV by virtue of the remarkable photo-thermal synergy. Consequently, a considerable syngas evolution rate of 180.9 mmol g_{cat}^{-1} h^{-1} has been achieved over Rh/InGaN$_{1-x}$O$_x$ NWs with an impressive selectivity of 96.3% under concentrated light illumination of 6 W cm^{-2} without other energy input. By coordinating the computational investigation, *in-situ* spectroscopic characterizations, and isotope experiments, it was discovered that the protons released from CH_4 dehydrogenation (induced by photoexcited holes) were reduced by photoexcited electrons toward H_2. The surface *C species from the eventual CH_4 dehydrogenation was then eliminated by the O atoms in Rh/InGaN$_{1-x}$O$_x$, thus contributed to the formation of CO and to the inhibition of coke deposition. The resultant O vacancies in Rh/InGaN$_{1-x}$O$_x$ can be further replenished by the C=O bond cleavage of CO_2, enabling an ideal chemical loop. As a result, a marked TON of 4182 mol syngas per mole Rh was obtained after six reuse cycles without obvious activity degradation. Overall, this work develops a promising nanoarchitecture for light-driven green syngas production by feeding two greenhouse gases i.e., CH_4 and CO_2.

Conflict of interest

The authors declare that they have no conflict of interest.

Acknowledgments

The work was supported by the National Natural Science Foundation of China (22109095), the Oceanic Interdisciplinary Program of Shanghai Jiao Tong University (SL2022MS007), Shanghai Pilot Program for Basic Research-Shanghai Jiao Tong University (21TQ1400207), the National Key Research and Development Program of China (2023YFB4004900), and Shanghai Municipal Science and Technology Major Project. This work was supported by the Natural Sciences and Engineering Research Council of Canada (NSERC)-RGPIN-2021-04250 and Centre Energie, Matériaux et Télécommunications, Institut National de la Recherche Scientifique (INRS)-Université du Québec.

Author contributions

Yixin Li and Baowen Zhou conceived the project. Yixin Li finished the whole experimental research and contributed to the DFT calculations. Syed M. Najib Hasan, Shamsul Arafin, and Sharif Md. Sadaf contributed to the growth of the supporting material. Yixin Li, Jinglin Li, Tianqi Yu, and Liang Qiu participated in the analysis of the experimental data. Yixin Li and Baowen Zhou wrote the paper with contributions from all co-authors. Lin Yao, Lei Zhu, and Sharif Md. Sadaf polished the writing. Baowen Zhou. leaded the research.

Appendix A. Supplementary material

Supplementary materials to this article can be found online at https://doi.org/10.1016/j.scib.2024.02.020.

References

[1] Groenigen V, Van KG, Kessel C, et al. Increased greenhouse-gas intensity of rice production under future atmospheric conditions. Nat Clim Chang 2013;3:288–91.
[2] Usman M, Daud WW, Abbas F. Dry reforming of methane: influence of process parameters—a review. Renew Sust Energ Rev 2015;45:710–44.
[3] Palmer C, Upham DC, Smart S, et al. Dry reforming of methane catalysed by molten metal alloys. Nat Catal 2020;3:83–9.
[4] Chen BZ, Chen FH, Ciais P, et al. Challenges to achieve carbon neutrality of China by 2060: status and perspectives. Sci Bull 2022;67:2030–5.
[5] Chen G, Waterhouse GI, Shi R, et al. From solar energy to fuels: recent advances in light-driven C1 chemistry. Angew Chem Int Ed 2019;58:17528–51.
[6] Zhou L, Martirez JMP, Finzel J, et al. Light-driven methane dry reforming with single atomic site antenna-reactor plasmonic photocatalysts. Nat Energy 2020;5:61–70.
[7] Hou Q, Li Y, Wu J, et al. Extraordinary catalytic performance of nickel half-metal clusters for light-driven dry reforming of methane. Adv Energy Mater 2023. https://doi.org/10.1002/aenm.202300071.
[8] Sheng L, Dong J, Zhou B. Formation of C-X bonds in CO_2 chemical fixation catalyzed by metal–organic frameworks. Adv Mater 2020;1806163.
[9] Dhandole LK, Kim SH, Moon G-h. Understanding (photo) electrocatalysis for the conversion of methane to valuable chemicals through partial oxidation processes. J Mater Chem A 2022;10:19107–28.
[10] Meng X, Cui X, Rajan NP, et al. Direct methane conversion under mild condition by thermo-, electro-, or photocatalysis. Chem 2019;5:2296–325.
[11] Hong J, Xu C, Deng B, et al. Photothermal chemistry based on solar energy: from synergistic effects to practical applications. Adv Sci 2022;9:2103926.
[12] Chung W, Tsao I, Chang M. Novel plasma photocatalysis process for syngas generation via dry reforming of methane. Energy Convers Manag 2018;164:417–28.
[13] Zhou W, Wang B, Tang L, et al. Photocatalytic dry reforming of methane enhanced by "dual-path" strategy with excellent low-temperature catalytic performance. Adv Funct Mater 2023. https://doi.org/10.1002/adfm.202214068.
[14] Tavasoli A, Gouda A, Zähringer T, et al. Enhanced hybrid photocatalytic dry reforming using a phosphated Ni-CeO_2 nanorod heterostructure. Nat Commun 2023;14:1435.
[15] Shoji S, Peng X, Yamaguchi A, et al. Photocatalytic uphill conversion of natural gas beyond the limitation of thermal reaction systems. Nat Catal 2020;3:148–53.
[16] Kushida M, Yamaguchi A, Miyauchi M. Photocatalytic dry reforming of methane by rhodium supported monoclinic TiO_2-B nanobelts. J Energy Chem 2022;71:562–71.
[17] Lorber K, Zavašnik J, Sancho-Parramon J, et al. On the mechanism of visible-light accelerated methane dry reforming reaction over Ni/CeO_{2-x} catalysts. Appl Catal B 2022;301:120745.
[18] Mahmodi G, Sharifnia S, Rahimpour F, et al. Photocatalytic conversion of CO_2 and CH_4 using ZnO coated mesh: effect of operational parameters and optimization. Sol Energy Mater Sol Cells 2013;111:31–40.
[19] Song Y, Ozdemir E, Ramesh S, et al. Dry reforming of methane by stable Ni–Mo nanocatalysts on single-crystalline MgO. Science 2020;367:777–81.
[20] Habisreutinger S, Schmidt M, Stolarczyk J. Photocatalytic reduction of CO_2 on TiO_2 and other semiconductors. Angew Chem Int Edit 2013;52:7372–408.
[21] Baharudin L, Rahmat N, Othman N, et al. Formation, control, and elimination of carbon on Ni-based catalyst during CO_2 and CH_4 conversion via dry reforming process: a review. J CO2 Util 2022;61:102050.
[22] Kim S, Lauterbach J, Sasmaz E. Yolk-Shell Pt-NiCe@SiO_2 single-atom-alloy catalysts for low-temperature dry reforming of methane. ACS Catal 2021;11:8247–60.
[23] Yang Y, Chai Z, Qin X, et al. Light-induced redox looping of a rhodium/Ce_xWO_3 photocatalyst for highly active and robust dry reforming of methane. Angew Chem Int Edit 2022;134:e202200567.

[24] Jiménez J, Betancourt L, Danielis M, et al. Identification of highly selective surface pathways for methane dry reforming using mechanochemical synthesis of Pd–CeO_2. ACS Catal 2022;12:12809–22.
[25] Vanka S, Zhou B, Awni A, et al. InGaN/Si double-junction photocathode for unassisted solar water splitting. ACS Energy Lett 2020;5:3741–51.
[26] Kibria M, Nguyen H, Cui K, et al. One-step overall water splitting under visible light using multiband InGaN/GaN nanowire heterostructures. ACS Nano 2013;7:7886–93.
[27] Zhou P, Navid I, Ma Y, et al. Solar-to-hydrogen efficiency of more than 9% in photocatalytic water splitting. Nature 2023;613:66–70.
[28] Zhou B, Ma Y, Ou P, et al. Light-driven synthesis of C_2H_6 from CO_2 and H_2O on a bimetallic AuIr composite supported on InGaN nanowires. Nat Catal 2023;6:987–95.
[29] Rashid R, Chen Y, Liu X, et al. Tunable green syngas generation from CO_2 and H_2O with sunlight as the only energy input. Proc Natl Acad Sci USA 2022;119.
[30] Wang Y, Wu Y, Sun K, et al. A quadruple-band metal–nitride nanowire artificial photosynthesis system for high efficiency photocatalytic overall solar water splitting. Mater Horizons 2019;6:1454–62.
[31] Lin J, Wang W, Li G. Modulating surface/interface structure of emerging InGaN nanowires for efficient photoelectrochemical water splitting. Adv Funct Mater 2020;30:2005677.
[32] Sadaf SM, Ra YH, Nguyen H, et al. Alternating-current InGaN/GaN tunnel junction nanowire white-light emitting diodes. Nano lett 2015;15:6696–701.
[33] Wang H, Qi H, Sun X, et al. High quantum efficiency of hydrogen production from methanol aqueous solution with PtCu-TiO_2 photocatalysts. Nat Mater 2023;22:1–8.
[34] Kresse G, Joubert D. From ultrasoft pseudopotentials to the projector augmented-wave method. Phys Rev B 1999;59:1758.
[35] Kresse G, Furthmüller J. Efficient iterative schemes for *ab initio* total-energy calculations using a plane-wave basis set. Phys Rev B 1996;54:11169.
[36] Blöchl PE. Projector augmented-wave method. Phys Rev B 1994;50:17953.
[37] Perdew JP, Burke K, Ernzerhof M. Generalized gradient approximation made simple. Phys Rev Lett 1996;77:3865.
[38] Perdew JP, Chevary JA, Vosko SH, et al. Atoms, molecules, solids, and surfaces: applications of the generalized gradient approximation for exchange and correlation. Phys Rev B 1992;46:66–71.
[39] Monkhorst HJ, Pack JD. Special points for Brillouin-zone integrations. Phys Rev B 1976;13:51–88.
[40] Shen D, Li Z, Shan J, et al. Synergistic Pt-CeO_2 interface boosting low temperature dry reforming of methane. Appl Catal B 2022;318:121809.
[41] Schaff W, Chen X, Hao D, et al. Electrical properties of InGaN grown by molecular beam epitaxy. Phys Status Solidi B Basic Res 2008;245:868–72.
[42] Feng X, Wang P, Hou J, et al. Significantly enhanced visible light photocatalytic efficiency of phosphorus doped TiO_2 with surface oxygen vacancies for ciprofloxacin degradation: synergistic effect and intermediates analysis. J Hazard Mater 2018;351:196–205.
[43] Lin J, Zhang Z, Chai J, et al. Highly efficient InGaN nanorods photoelectrode by constructing Z-scheme charge transfer system for unbiased water splitting. Small 2021;17:2006666.
[44] Li J, Sheng B, Chen Y, et al. Oxynitride-surface engineering of rhodium-decorated gallium nitride for efficient thermocatalytic hydrogenation of carbon dioxide to carbon monoxide. Chem Commun 2022;5:107.
[45] Hu D, Ordomsky V, Khodakov A. Major routes in the photocatalytic methane conversion into chemicals and fuels under mild conditions. Appl Catal B 2021;286:119913.
[46] Choi W, Termin A, Hoffmann MR. The role of metal ion dopants in quantum-sized TiO_2: correlation between photoreactivity and charge carrier recombination dynamics. J Phys Chem C 2002;98:13669–79.
[47] Doghachi A, Faris A, Jassim Ali FA, et al. Enhancement of CO_2 reforming of CH_4 reaction using Ni, Pd, Pt/$Mg_{1-x}Ce_x^{4+}O$ and Ni/$Mg_{1-x}Ce_x^{4+}O$ catalysts. Catalysts 2022;10:1240.
[48] Jiang Y, Li S, Wang S, et al. Enabling specific photocatalytic methane oxidation by controlling free radical type. J Am Chem Soc 2023;145:2698–707.
[49] Bu K, Kuboon S, Deng J, et al. Methane dry reforming over boron nitride interface-confined and LDHs-derived Ni catalysts. Appl Catal B 2019;252:86–97.
[50] Miao C, Chen S, Shang K, et al. Highly active Ni–Ru bimetallic catalyst integrated with MFI zeolite-loaded cerium zirconium oxide for dry reforming of methane. ACS Appl Mater Interfaces 2022;14:47616–32.
[51] Yan Z, Liu Q, Liang L, et al. Surface hydroxyls mediated CO_2 methanation at ambient pressure over attapulgite-loaded Ni-TiO_2 composite catalysts with high activity and reuse ability. J CO2 Util 2021;47:10148.
[52] Song H, Meng X, Wang S, et al. Direct and selective photocatalytic oxidation of CH_4 to oxygenates with O_2 on cocatalysts/ZnO at room temperature in water. J Am Chem Soc 2019;141:20507–15.

Yixin Li is currently a Ph.D. candidate in Prof. Baowen Zhou's group at the School of Mechanical Engineering, Shanghai Jiao Tong University. His research interest is focused on methane conversion and solid oxide electrolysis cell.

Lin Yao is currently an Associate Professor in China-UK Low Carbon College, Shanghai Jiao Tong University. Her research interest is focused on small materials, green hydrogen, and methane conversion.

Shamsul Arafin is an Assistant Professor at the Electrical and Computer Engineering Department, The Ohio State University (OSU). He is focusing on the area of photonic integrated circuits, semiconductor lasers, quantum photonics, III-V compound semiconductor materials.

Sharif Md. Sadaf is currently an Assistant Professor at the Energy, Materials and Telecommunications research center at the Institut national de la recherche scientifique (INRS). His research interest and expertise sit in the exciting space between materials science, electrical engineering, and applied physics. He is an expert on the epitaxial nanomaterials growth by molecular beam epitaxy) and pulsed laser deposition, nanofabrication and characterizations for nanoelectronic and nanophotonic devices.

Baowen Zhou is currently an Associate Professor at the School of Mechanical Engineering, Shanghai Jiao Tong University. His research interest is focused on artificial photosynthesis, green hydrogen, renewable synthetic fuels, energy storage and green power.